[1]Dr. C. Suresh,

[2]Dr. S. S. Nagamuthu Krishnan,

[3]Rashima Mahajan,

[4]Dr. Ravi Kumar Tata

[5]Dr. Shankar N,

[6]Dr. R. Ramkumar

Optimizing Osteoporosis Classification through Femur Bone Volumetric Estimation with Deep Belief Network in X-ray Imaging

Abstract: **-** The accurate classification of osteoporosis is a crucial requirement in the medical field for identifying patients with skeletal disorders associated with aging. Achieving improved accuracy and reduced computational complexity in classification algorithms is essential. To address this, our research proposes a novel classification method utilizing the Hybrid Gradient Particle Swarm (HSG) Optimization-based Deep Belief Network, integrating the Particle Swarm Optimization (PSO) algorithm into the Gradient Descent (GD) algorithm. The osteoporosis classification process comprises five key steps: Preprocessing, Active Shape Model-based Segmentation, Geometric Estimation employing the proposed template search method, Feature Extraction for extracting medical and image-level features, and Osteoporosis Classification using the HSG-based Deep Belief Network. The proposed template search method efficiently and automatically updates the geometric points of the femur segment. Experimental validation using a real-time database demonstrates the effectiveness of the proposed method in terms of accuracy, sensitivity, and specificity. The results indicate an accuracy of 0.9724, affirming the efficacy of the proposed algorithm in making precise decisions regarding osteoporosis classification.

Keywords: Femur bone, Osteoporosis classification, Deep Belief Network, Particle Swarm Optimization, Gradient search algorithm

I. INTRODUCTION

The examination of the National Health and Nutrition Examination Survey (NHANES III) indicated that around 14 million women aged 50 years and above suffer from low bone density [9]. According to the World Health Organization (WHO), approximately 70% of women are affected by osteoporosis, posing a significant challenge in diagnosis and femur fracture prevention [7]. Osteoporosis, emerging as a global health concern, leads to substantial mortality and morbidity [13] [3]. Current diagnostic methods involve a prolonged preclinical phase and lack cost-effective therapeutic options [14] [3]. The condition severely impacts bone density, increasing the risk of fractures due to bone fragility [14]. Termed the "silent epidemic," osteoporosis often remains undiagnosed until fractures, particularly in the hip region, occur, significantly affecting the quality of life [13]. Fractures can also impact vertebrae, causing height loss, severe backache, and bone deformities. Early detection remains the primary means of addressing osteoporosis-related fractures [15] [3].

The objective of the proposed diagnostic method is to determine whether a patient is affected by osteoporosis, offering the possibility to increase bone mineral density and reduce the risk of fractures. Diagnosis typically

[1] [1]Professor, Department of Electrical and Electronics Engineering, School of Engineering and Technology, Dhanalakshmi Srinivasan University, Trichy, Tamilnadu, India sureshc.set@dsuniversity.ac.in

[2]Senior Assistant Professor, Department of Computer science and Engineering,

SASTRA Deemed University, Kumbakonam, Tamilnadu, India. ssnkrishnan@gmail.com

[3]Professor, Department of Computer Science and Engineering , Manav Rachna International Institute of Research and Studies, Faridabad , India. rashimamahajan24@gmail.com

[4]Associate Professor, Department of Computer Science and Engineering, Koneru Lakshmaiah Education Foundation, Vaddeswaram, Andhra Pradesh, India. rktata5860@gmail.com

[5]Associate Professor, Department of Biomedical Engineering, School of Engineering and Technology, Dhanalakshmi Srinivasan University, Trichy. bmeshankar@gmail.com

[6]Assistant professor, Department of Electrical and Electronics Engineering, School of Engineering and Technology, Dhanalakshmi Srinivasan University, Trichy, Tamilnadu, India. 2019ramkr@gmail.com

Corresponding author: Dr. C. Suresh sureshc.set@dsuniversity.ac.in

involves X-rays, assisted by CT images and volumetric Quantitative Computed Tomography (vQCT) techniques [8]. Clinical trials employ traditional methods to assess bone mineral content, analyzing bone size, shape, and structure parameters to reveal bone quality, particularly in evaluating the proximal femur, which presents challenges due to anatomical complexity [16] [10]. Image processing methods analyze proximal femur architecture to uncover femoral neck and trochanteric volumes for densitometry and geometry analysis [11]. Factors influencing fracture risk, such as areal bone densities, are associated with osteoporosis [12].

Patients with osteoporosis undergo non-invasive assessment of bone using Bone Mineral Density (BMD), which, when associated with femoral geometry, predicts breaking strength more effectively than BMD alone [17] [8]. BMD is obtained through various methods, including QCT, Dual-energy X-Ray Absorptiometry (DXA), and ultrasound, with DXA T-score being the WHO-defined measure for osteoporosis [18] [3]. BMD is measured in areal and volume density, where Areal Bone Mineral Density (aBMD) and Volumetric Bone Mineral Density (vBMD) are crucial parameters. aBMD is influenced by sex, body size, quality, geometry, and composition [17] [20] [19] [8]. While BMD comparison with reference mean BMD is common, BMD alone does not suffice to predict fractures [4].

This research aims to develop a technique for Osteoporosis classification based on femur bone volumetric estimation. The proposed method comprises five steps: pre-processing, femur boundary segmentation, femoral geometry measurement, feature extraction, and classification. The input X-Ray image undergoes pre-processing through ROI-extraction to enhance processing efficiency and reduce complexity. Femur boundary segmentation uses the active shape model on the pre-processed image to extract the femur. Femoral geometry measurement employs the proposed template search method to estimate geometric points using the femur. Important features, both medical and image-level, are then extracted from the detected geometric points. Medical level features include hip axis length, femoral neck axis length, femoral head diameter, femoral neck width, neck shaft angle, and shaft width. Image level features such as mean, variance, entropy, skewness, and kurtosis are extracted from the segmented image. The extracted features form a feature vector applied to the proposed Hybrid Particle Swarm Optimization with Gradient Descent based Deep Belief Network (HSG-DBN) for classification into three classes: normal, osteopenia, and osteoporosis.

The contributions of this paper include the introduction of the proposed template search method, enabling automatic estimation of geometric points for effective extraction of medical features for Osteoporosis classification. Furthermore, the paper presents the use of HSG-DBN for Osteoporosis classification, integrating gradient descent and Particle Swarm Optimization (PSO) for optimal DBN training, with the optimization developed using the proposed HSG algorithm.

The paper is organized as follows: Section 1 provides the background, Section 2 covers literature review and existing method challenges, Section 3 outlines the proposed method, Section 4 presents the results, and Section 5 concludes the paper.

Motivation

The section depicts the literature review and challenges of the existing method.

2.1 Literature Survey

In their work [1], Jennifer S. Gregory and Richard M. Aspden devised Femoral geometry measurements to assess an individual's hip fracture risk. However, a drawback of this method lies in its limited accuracy in predicting fracture risk. Melih S. Aslan et al. [2] introduced a method called Probabilistic and universal shape model, which demonstrated robustness under varying noise levels and high reliability irrespective of bone diseases. Despite these advantages, the method entails high computational effort and is unable to mitigate misclassifications. Esther Pompe et al. [3] presented a Manual vertebral bone attenuation measurement method for estimating femur bone volumetric, ensuring early osteoporosis detection on low-dose chest CT with good reliability but offering lower precision. Sami P. Vaananen et al. [4] developed Statistical appearance models (sams) and Finite Element (FE) models for accurate reconstruction of femur shape, internal density, and thickness. However, the method lacks the potential to reduce computation time using graphical processor unit calculations. V. Sapthagirivasan et al. [5] introduced the Trabecular Enrichment Approach (TEA), effective for identifying women vulnerable to

osteoporotic risk but sensitive to manual control. Alexandra Hotca et al. [6] proposed the Bical (Bias Calculation) method, offering improved precision but facing challenges due to poor contrast and relatively low Signal-to-Noise Ratio (SNR). Furthermore, standard automatic segmentation algorithms struggle with disease detection. Ludovic Humbert et al. [7] devised a model named Statistical shape and appearance model with a 3D-2D registration approach, enhancing the osteoporosis detection process while maintaining DXA as the standard routine modality. However, the accuracy of the method remains poor, and it is time-consuming. Kiattisin Supaporn and Chamnongthai Kosin [8] introduced the Active contour model (ACM), effective in estimating Bone Mineral Density (BMD) for osteoporosis diagnosis from a single x-ray image. Nonetheless, the method comes with a high equipment cost.

2.2 Challenges

- The limitations associated with Quantitative CT (QCT) and DXA imaging include their reliance on high radiation doses and the substantial equipment costs, albeit these machines are commonly available in hospital settings [1] [8].
- DXA encounters challenges in analyzing calcifications, overlying soft tissue, and fails to capture 3D bone properties, leading to inaccuracies [8]. As a low-resolution technique, DXA falls short in assessing bone microarchitecture crucial for defining osteoporosis [6].
- T-score, Hip Structural Analysis (HSA), dual-energy x-ray absorptiometry (DXA)-based finite element analysis, and fracture risk assessment tool (FRAX) overlook the 3D distribution of cortical and trabecular bone mass in bone [14-16] [7].
- The automated point correspondence detection algorithm, Scale-Invariant Feature Transform (SIFT) [2], proves inadequate in detecting Vertebral Body (VB) height changes, resulting in the failure to scan patients at regular intervals for identifying corresponding points.
- Trabecular Enrichment Approach (TEA) [5] faces challenges related to spatial resolution and struggles in finalizing the Region of Interest (ROI), crucial for locating the gap between the femur head region and the acetabulum.

3 Proposed Method of Osteoporosis Classification Using The HSG-Based Deep Belief Network in X-Ray Images.

Osteoporosis is a condition characterized by weakened bones, making them prone to fractures, a vulnerability easily identifiable through X-ray examinations. The affected bones exhibit larger spaces and holes compared to their stronger, normal counterparts, a result of hormonal changes affecting both men and women. Early and automatic detection of osteoporosis is crucial, and X-ray images of femur bones serve as a valuable diagnostic tool. The proposed classification method is based on femur bone volumetric estimation, involving five consecutive steps. In Step 1, interesting regions are extracted from the X-ray femur image through a segmentation process. This process delineates femur boundaries from the pre-processed X-ray image using the active shape model. The third step involves femoral geometry measurement, where femoral points are automatically marked using the proposed template search method. In the fourth step, features are extracted from the marked femur. Finally, classification is carried out using the proposed HSG-DBN, determining whether the patient is affected by osteoporosis or not, with the assigned class labels being normal, osteopenia, or osteoporosis. Figure 1 illustrates the block diagram of the proposed automated method for osteoporosis classification.

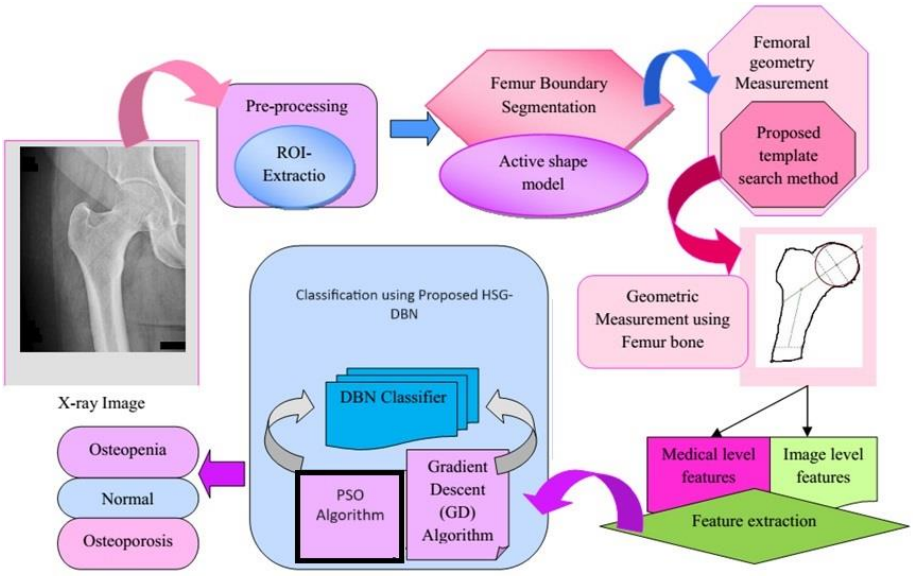

Figure 1. Block diagram of the proposed method of osteoporosis classification using Femur bone volumetric estimation

3.1 Pre-processing

The initial stage in Femur bone volumetric estimation is pre-processing, which prepares the X-ray image for subsequent processing by eliminating any complexities. This involves extracting regions of interest from the input X-ray image.

3.2 Femur boundary segmentation using active shape model

Active Shape Modelling (ASM), as described in [23], is a technique that characterizes object boundaries using a set of points, each representing a specific region within the object. Statistical analysis of these points yields the primary model of variation for a new shape. The initial approximation for any shape is established through training with a few images, determining the optimal orientation, shape, and position. When a new image is introduced, the shape of the image is extracted based on the prior training. ASM shares similarities with the active contour model but distinguishes itself through global shape constraints that elucidate the spatial location of the object. Particularly applicable to medical images, ASM excels in extracting shapes. In this paper, the femur's shape is acquired, facilitating the identification of significant femur points for subsequent feature extraction.

ASM offers the advantages of detecting all edges and efficiently distinguishing bone structures from X-rays, surpassing other methods in this aspect. The extraction of bone shape is effectively handled, making ASM well-suited for various bone orientations. The lines connecting statistical points do not contribute to the shape, and the distance between points is determined by Euclidean distance. Consequently, the distance between shapes relies on Euclidean distance, represented as:

$$E = \sqrt{(p_2 - p_1)^2 + (q_2 - q_1)^2} \tag{1}$$

In the context of aligning two points, denoted as p and q, the computation of centroids plays a crucial role. Centroids are determined as the mean of the positions of these points. The shape size, defined as the square root of the Euclidean distance between the points and the centroid, serves as a significant parameter for alignment. This shape size facilitates the automatic initialization of a test input femur image.

In the active shape model, the initial step involves learning the shape of the image through a training process. Alignment of various image shapes is necessary to generate the mean shape. Aligning the shape requires the extraction of all shapes within the x-ray at a specific orientation, allowing for the presence of the bone anywhere in the x-ray image. Orientation is a critical factor for locating the bone in x-ray images at varying angles, making

the method effective for bone segmentation. The desired shape is achieved based on its close match with the mean image, represented as:

$$\hat{u} = \bar{u} + \gamma c \tag{2}$$

where, $\hat{u}$ is the generated shape vector obtained using the active shape model, and $\bar{u}$ indicates the mean shape that is given as,

$$\bar{u} = \frac{1}{v_{shapes}} \sum_{t=1}^{v_{shapes}} u_t \tag{3}$$

γ symbolizes the Eigen vector of the covariance matrix M belonging to the training image shape points. The covariance matrix is given as,

$$M = \frac{1}{v_{shapes}-1} \sum_{t=1}^{v_{shapes}} \left(u_t - \bar{u}\right)\left(u_t - \bar{u}\right)^T \tag{4}$$

The significance of Eigen vectors derived from the covariance matrix, particularly those associated with the largest Eigen values, lies in representing highly meaningful modes of variation. By varying the value of c in equation (2), the optimal set of shapes is generated. Following the completion of training, the test image's shape is sought by comparing it with the mean shape. The bone's shape is determined by identifying the image that aligns with the mean shape. The distance between the test shape and the mean shape is quantified as:

$$\partial = \left(m - \bar{m}\right)^T M_m^{-1} \left(m - \bar{m}\right) \tag{5}$$

where, M_m^{-1} is the covariance matrix and $\bar{m}$ is the mean profile. The minimum distance yields the best shape, and the method of shape segmentation seems to be highly robust.

3.3 Femoral geometry measurement using the proposed template search method

This section underscores the importance of identifying key points on the femur bone through the proposed template search method for the computation of various medical-level features from the femur segment. The template search method, as proposed, automatically computes significant points within the femur segment, presenting advantages over existing manual marking methods. In a previous study [1], femur segment geometry estimation was conducted manually, which at times lacked precision and required prior knowledge of individual femurs for accurate marking. The variability in femur structure among individuals contributed to the limitations of manual marking. Therefore, the introduction of an automatic method employing the template search method for landmark identification adds significant value to the research. Accurate estimation of femoral geometry is crucial for defining the risk of fracture and assessing bone strength. Figure 2 illustrates the geometric measurement facilitated by the automatic template search method, and the subsequent steps outline the process involved in measuring the geometry of the femurs.

In the first step, the Circular Hough Transform is applied with the primary objective of detecting circular regions within the femur segment, aiming to identify the optimal center denoted as O in Figure 2. The Circular Hough Transform facilitates the localization of circular regions, enabling precise identification of the circle's center.

Moving on to the second step, points B and G are determined. Using O as the center, a horizontal line is drawn across the optimal center, and the points where it intersects the femoral boundary are marked as B and G. This step involves establishing key reference points on the femoral boundary concerning the optimal center.

The third step involves marking the point A. By measuring the distance between points B and G and dividing it by 8, a distance measure 'x' is obtained. Point B is then extended outward to point A, situated at a distance of 'x' from B. This establishes the position of point A in relation to the initial reference points.

Proceeding to the fourth step, a perpendicular bisector is drawn with O as the optimal center. This bisector is applied to the line segment connecting points A and G, resulting in the intersection points I and C. Additionally, a parallel line HD is drawn relative to the line IC, intersecting the femoral boundary at three points when a horizontal line is drawn from point H. This step enhances the geometric characterization of the femoral region.

Finally, in the fifth step, the point J is located. Connecting points E and F, which form the femoral shaft, a line is drawn from the midpoint of EF to intersect with the line AG at point J. The optimization of these points is efficiently computed using the proposed template search method. This method automatically derives crucial points from the femoral boundaries, ensuring the accurate computation of medical-level features for subsequent analysis.

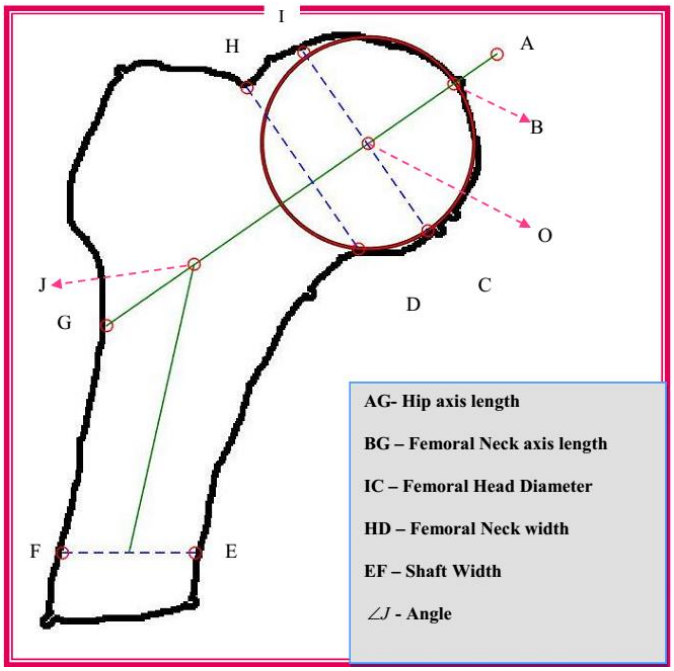

Figure 2. Proposed template search method for measuring the femoral geometry

3.4 Feature extraction using the medical level and image level features

This section focuses on extracting features through both medical and image-level parameters. The geometric points, automatically detected through the proposed automatic template search method, contribute to obtaining medical level features. Simultaneously, the pixels encompassed by these medical level features form the basis for extracting image-level features.

3.4.1 Medical level features: Effective classification heavily relies on medical level features, significantly contributing to improved classification accuracy. These crucial medical level features comprise hip axis length, femoral neck axis length (HAL), femoral head diameter (FHD), femoral neck width (FNW), neck shaft angle (NSA), and shaft width (w). Extraction of these features is accomplished using geometric points obtained through the automated template search method.

a) Hip Axis Length (HAL): This refers to the distance between the greater trochanter (point A) and the inner pelvic brim (point G) as illustrated in Figure 2. HAL is a crucial measurement associated with bone health, where a longer HAL indicates a higher risk of fractures, serving as a reliable indicator of bone diseases.

b) Femoral Neck Axis Length (FNAL): FNAL is defined as the distance between the greater trochanter (point B) and the apex of the femoral head (point G), as shown in Figure 2. This measurement is particularly relevant when femurs are isolated from connective tissues and lack association with the pelvic region.

c) Femoral Head Diameter (FHD): FHD measures the strength of the bone and corresponds to the distance between geometric points I and C in Figure 2. Maximizing the femoral head diameter is essential for enhancing bone strength.

d) Femoral Neck Width (FNW): FNW is the narrowest distance across the femoral neck, perpendicular to the neck axis. This distance, depicted as the line between points F and G in Figure 2, is indicative of bone damage risk, with a lower FNW suggesting a higher risk. However, it's important to note that FNW is influenced by factors such as age, body size, and other parameters.

e) NSA: The neck shaft angle, designated as $\angle J$, represents the angle between the femoral neck axis and the shaft axis. The normal NSA is found to be about $120° - 135°$ in adults, and it varies for individuals based on their physical activity.

f) Shaft width: The dimension of the femur immediately beneath the trochanter minor is identified as the shaft width. In Figure 2, the line EF illustrates the measurement of the shaft width.

3.4.2 Image level features: Pixel-wise estimation is employed to derive image-level features, encompassing mean, variance, entropy, skewness, and kurtosis. The mean feature is mathematically expressed as follows:

$$\mu = \frac{1}{n}\sum_{i=1}^{n}\rho_i \tag{6}$$

where, μ is the mean, ρ_i refers to the i^{th} pixel of the femur image, and n be the total number of pixels in the image. The significance of computing the mean lies in the extraction of texture features from the femur image to enhance the classification accuracy. The determination of image variance is accomplished as follows,

$$V = = \frac{1}{n}\sum_{i=1}^{n}\left(\rho_i - \mu\right)^2 \tag{7}$$

where, V is the variance feature of the femur image. The entropy-based feature is computed as,

$$e\left(\rho_i\right) = \sum_{i=1}^{U(\rho_i)} \mathrm{P}_i \log \mathrm{P}_i \tag{8}$$

where, $U\left(\rho_i\right)$ is the unique pixel values of the femur image. The entropy computation is based on the pixel intensity and the entropy value is large when the difference in the intensity of the neighboring pixels is large. Skewness is the measure of asymmetry and kurtosis is the measure of the heavy or light-tailed parameter based on the normal distribution. The skewness and kurtosis are denoted as, S and K .

The feature vector of the femur image is the combination of the medical features and image-level features that is given as,

$$F = \left\{f_1, f_2, ..., f_j, ..., f_l\right\} \tag{9}$$

where, l is the total number of features for an femur segment and is equal to 11 such that the dimension of the feature vector for the individual femur segment is given as, $\left[1 \times 11\right]$. The features of the femur segment $f_1, f_2, ..., f_{11}$ are the HAL, FNAL, FHD, FNW, NSA, w, μ , V , $e\left(\rho_i\right)$, S , and K . HAL, FNAL, FHD, FNW, NSA, and w are the medical-level images and μ , V , $e\left(\rho_i\right)$, S , and K are the image-level features.

3.5 Classification using the proposed GHS-DBN for Osteoporosis

The proposed HSG-DBN is developed by training the DBN [21, 22] using the Particle Swarm Optimization Algorithm along with the Gradient Descent Algorithm based on the error estimate.

The PSO algorithm relies on the concept of musicians tuning their instruments to achieve harmony. During the search for optimal pitch, a solution vector is constructed, where individual decision variables explore solutions within a defined range. When a better solution is identified, it is stored in memory. The advantages of the PSO algorithm include: i) lower mathematical requirements compared to other optimization algorithms, eliminating the need to set initial values for decision variables, ii) no requirement for derivative information, iii) enhanced flexibility as it generates a new vector by considering all available existing vectors, and iv) efficient determination of high-performance spaces in less time. However, similar to other optimization problems, PSO has the drawback of converging to local optimal regions when dealing with multimodal issues. Gradient descent's simplicity and lack of a need for second derivative derivation contribute to fast computation and minimal storage requirements. Nevertheless, the scalability of the problem is a limitation for GD. The demerits of PSO and GD are balanced in the proposed HSG algorithm, which focuses on the optimal tuning of Deep Belief Network (DBN) weights.

3.5.1 Architecture of DBN:

The significance attributed to Deep Belief Networks (DBN) [22] lies in its capability to ensure robust classification of input data by efficiently utilizing hidden neurons. It possesses the inherent capacity to comprehend the intricacies within the data for achieving effective classification. To advance the classification process, the features extracted from the input image are input to the classifier, which then determines the class label using the GHS algorithm for training. The DBN architecture comprises multiple Restricted Boltzmann Machines (RBMs) and a Multi-Layer Perceptron (MLP) layer, with two RBMs employed in this specific configuration. The MLP layer mirrors a neural network structure with input, hidden, and output layers. The features undergo processing through the weights connecting these layers. The feature vector serves as input for RBM1, and the output from RBM1 becomes the input for RBM2. The output from RBM2 serves as input to the MLP layer, ultimately determining the class label for the given input data. Figure 3 illustrates the DBN network architecture trained using the HS algorithm. The DBN output, represented by the class label, categorizes the input femur segment as normal, osteopenia, or osteoporosis, enabling the identification of individuals affected by osteoporosis. The automated detection method ensures prompt and effective decision-making in osteoporosis diagnosis.

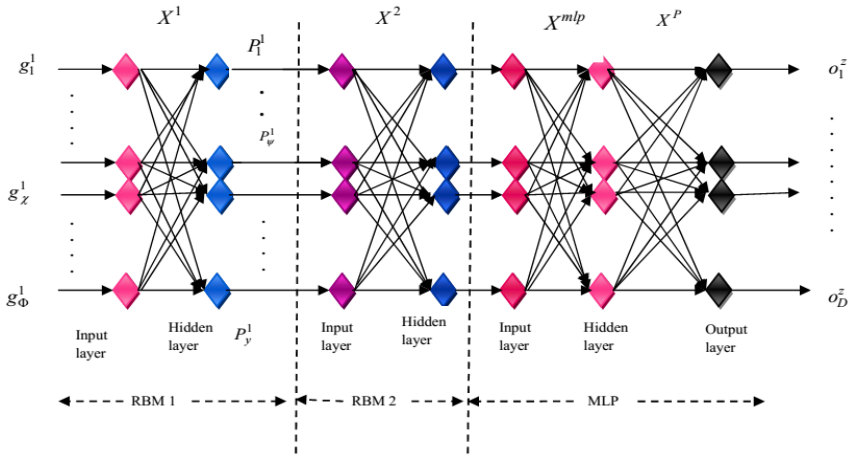

Figure 3. Architecture of DBN model

The mathematical representation of DBN is given below: The input feature vector is the input to the input layer of RBM1, and the neurons present in the input layer is given as,

$$g^1 = \{g_1^1, g_2^1, g_3^1, \ldots, g_\chi^1, \ldots, g_\Phi^1\}; \quad 1 \le \chi \le \Phi; \qquad \Phi = (1 \times 11) \tag{10}$$

$$d^1 = \{d_1^1, d_2^1, \ldots, d_\psi^1, \ldots, d_y^1\}; \; 1 \le \psi \le y \tag{11}$$

where, N_χ^1 is the χ^{th} input neuron of RBM1 and there are 11 input neurons that equals to the total number of input features corresponding to the individual pixels of the image. M_ψ^1 is the ψ^{th} hidden neuron of RBM1 and

there are y number of hidden neurons in RBM1. Let q and s represent the biases in the visible, and the hidden layer that is given as,

$$q^1 = \{q_1^1, q_2^1, q_3^1, \ldots, q_\chi^1, \ldots, q_\Phi^1\} \tag{12}$$

$$s^1 = \{s_1^1, s_2^1, \ldots, s_\psi^1, \ldots, s_y^1\} \tag{13}$$

The biases in input and hidden layer of RBM1 are equal to the number of hidden and input neurons in the layer. The weights of RBM1 are given as,

$$X^1 = \left\{X_{\chi\psi}^1\right\}; 1 \le \chi \le \Phi; 1 \le \psi \le y \tag{14}$$

where, $X_{\chi\psi}^1$ is the weights between the χ^{th} input neuron and the ψ^{th} hidden neuron and the dimension of the weights in RBM1 is given as, $[\Phi \times y]$. Therefore, based on the biases and the weights, the hidden layer output from RBM1 is given as,

$$P_\psi^1 = \sigma\left[q_\psi^1 + \sum_\chi g_\chi^1 \, X_{\chi\psi}^1\right] \tag{15}$$

where, σ is the activation function in RBM1. Hence, the output of RBM1 is represented as,

$$P^1 = \{P_\psi^1\}; 1 \le \psi \le y \tag{16}$$

The output from the RBM1 forms the input to RBM2, and the output of RBM2 is computed similar to the above explained equations. The output from RBM2 is denoted as P_ψ^2 that forms the input to the MLP layer. The output from RBM2 is given as,

$$Q^z = \{Q_1^z, Q_2^z, \ldots, Q_\psi^z, \ldots, Q_y^z\} = \{h_\psi^2\}; 1 \le \psi \le y \tag{17}$$

where, y is the total number of input neurons in MLP. The hidden neurons of MLP is given as,

$$R^z = \{R_1^z, R_2^z, \ldots, R_\upsilon^z, \ldots, R_{\mathrm{N}}^z\}; \quad 1 \le \upsilon \le \mathrm{N} \tag{18}$$

where, N corresponds to the total number of hidden neurons in the MLP and X_υ^z represents the bias of υ^{th} hidden neuron and the output of MLP layer is given as,

$$o^z = \{o_1^z, o_2^z, \ldots, o_\partial^z, \ldots, o_D^z\}; \; 1 \le \partial \le D \tag{19}$$

where, D is the number of output neurons in MLP layer weight vector between the input layer, and the hidden layers and is represented as,

$$X^{mlp} = \{X_{\psi\upsilon}^{mlp}\}; \; 1 \le \psi \le y; 1 \le \upsilon \le \mathrm{N} \tag{20}$$

where, $X_{\psi\upsilon}^{mlp}$ is the weight vector among ψ^{th} input neuron, and υ^{th} hidden neuron. The output of the MLP hidden layer depends on the weight vectors of hidden neurons with the bias, which is given as,

$$I = \left[\sum_{\psi=1}^{y} X_{\psi\upsilon}^{mlp} \times l_\psi\right] X_\upsilon^z \; \forall l_\psi = P_\psi{}^2 \tag{21}$$

where, ϖ_υ^z is the bias. The weight vector between the hidden and the output layer is indicated as ω^M and is given by,

$$X^{M} = \{X_{\upsilon\partial}^{P}\};\ 1 \le \upsilon \le \mathrm{N};\ 1 \le \partial \le D \tag{22}$$

Thus, the output of MLP is computed as,

$$O_{\partial} = \sum_{\upsilon=1}^{\mathrm{N}} X_{\upsilon\partial}^{P} \times I \tag{23}$$

where, $X_{\upsilon\partial}^{M}$ denotes the weights between the υ^{th} hidden and ∂^{th} output neurons, and I is the output from the hidden layer.

a) During the training phase of the Restricted Boltzmann Machine (RBM) layer, the HSG algorithm is employed to advance the training process. This algorithm relies on minimizing energy, utilizing the weights associated with the minimum energy to update the RBM weights when computing the output.

b) In the training phase of the Multi-Layer Perceptron (MLP), the training process is conducted based on the proposed HSG algorithm. The optimal weights are determined using the HSG algorithm by minimizing the error. The algorithm that results in the minimum error value is then utilized to update the weights of the MLP. The following steps outline the training process of the MLP.

Step 1: Randomly generate the weight vectors X^{M} and X^{mlp} as shown in equations (22) and (20), respectively.

Step 2: Read the input vector P_{ψ}^{2} obtained from the output layer of RBM2.

Step 3: Calculate I and O_{∂} based on equations (21) and (23), respectively.

Step 4: Compute the error of the MLP layer that is obtained using the estimated and target output, given as,

$$\in^{a}_{avg} = \frac{1}{\aleph} \sum_{\mathrm{K}=1}^{\aleph} \left(O_{\partial} - ground\right) \tag{24}$$

where, O_{∂} is the attained output, and $ground$ is the expected output. Based on the minimum error, the weights are updated in DBN.

Step 5: Determine the weight vectors in the visible layer, and the hidden layers using the partial derivative as given below,

$$\Delta X_{\psi\upsilon}^{mlp} = -\eta \frac{\partial \in^{a}_{avg}}{\partial X_{\psi\upsilon}^{mlp}} \tag{25}$$

$$\Delta X_{\upsilon\partial}^{M} = -\eta \frac{\partial \in^{a}_{avg}}{\partial X_{\upsilon\partial}^{M}} \tag{26}$$

where, η is the learning rate.

Step 6: Determine the weights of the next iteration using the proposed algorithm as,

$$X_{\psi\upsilon}^{mlp}(t+1) = X_{\psi\upsilon}^{mlp}(t) \pm rand(0,1) \times \beta \tag{27}$$

where, $rand(\ )$ is the random number that varies in the interval $[0,1]$, and $X_{\psi\upsilon}^{mlp}(t)$ is the weight of the input and the hidden layer of MLP in the t^{th} iteration. Substituting the above equation in the weight update equation of Gradient search algorithm,

$$X_{\psi\upsilon}^{mlp}(t+1) = X_{\psi\upsilon}^{mlp}(t) + \Delta X \tag{28}$$

$$X_{\psi\upsilon}^{mlp}(t+1)=\frac{X_{\psi\upsilon}^{mlp}(t+1)+X_{\psi\upsilon}^{mlp}(t+1)}{2} \tag{29}$$

$$X_{\psi\upsilon}^{mlp}(t+1)=\frac{X_{\psi\upsilon}^{mlp}(t)\pm rand(0,1)\times\beta+X_{\psi\upsilon}^{mlp}(t)+\Delta X_{\psi\upsilon}^{mlp}}{2} \tag{30}$$

$$X_{\psi\upsilon}^{mlp}(t+1)=\frac{2X_{\psi\upsilon}^{mlp}(t)\pm rand(0,1)\times\beta+\Delta X_{\psi\upsilon}^{mlp}}{2} \tag{31}$$

where, $X_{\psi\upsilon}^{mlp}(t+1)$is the weight of the input and hidden layer of MLP in the $(t+1)^{th}$ iteration. The change in weights is denoted as, $\Delta X_{\psi\upsilon}^{mlp}$. The weight update of MLP between the hidden and output layer is given as,

$$X_{\upsilon\partial}^{M}(t+1)=\frac{2X_{\upsilon\partial}^{M}(t)\pm rand(0,1)\times\beta+\Delta X_{\upsilon\partial}^{M}}{2} \tag{32}$$

where, $X_{\upsilon\partial}^{M}(t+1)$ is the weight update between the hidden and the output layers of MLP in the $(t+1)^{th}$ iteration and $X_{\upsilon\partial}^{M}(t)$is the weight update between the hidden and output layer of MLP in the t^{th} iteration or the previous iteration and ΔX is the change in the weights between the hidden and output layer of MLP. The weight update follows the minimum error estimate.

Step 7: Repeat steps 2 to 6, until the best weight vector is determined.

4. Results and Discussion

This section presents the outcomes and discussion of the proposed osteoporosis detection method, emphasizing the effectiveness of the approach through a comprehensive comparative analysis.

4.1 Experimental setup

The Osteoporosis classification technique proposed in this study has been executed in MATLAB, utilizing a real-time database. The MATLAB implementation is carried out on a personal computer running the Windows 8 operating system.

4.2 Database employed

The study utilized a real-time database constructed with data gathered from individuals residing in the Chennai locality. X-ray images from approximately 50 individuals within the age range of 25-81 years were collected for the purpose of osteoporosis classification. The database comprises a total of 50 women and 50 men, highlighting the significant impact of osteoporosis on elderly patients. Ethics approval for the study was obtained from the affiliated university.

4.3 Experimental Analysis

Figure 4 displays a representative outcome of the conducted experiment. The experiment involved the analysis of 50 images, and within this set, this section illustrates the experimental results for a single image. The original image utilized for the analysis is presented in Figure 4a), followed by the application of the active shape model, as depicted in Figure 4b). Finally, Figure 4c) showcases the results of the geometric estimation achieved through the proposed template model. The identification of geometric points is crucial for subsequent medical feature extraction and, consequently, for extracting image-level features to facilitate effective classification.

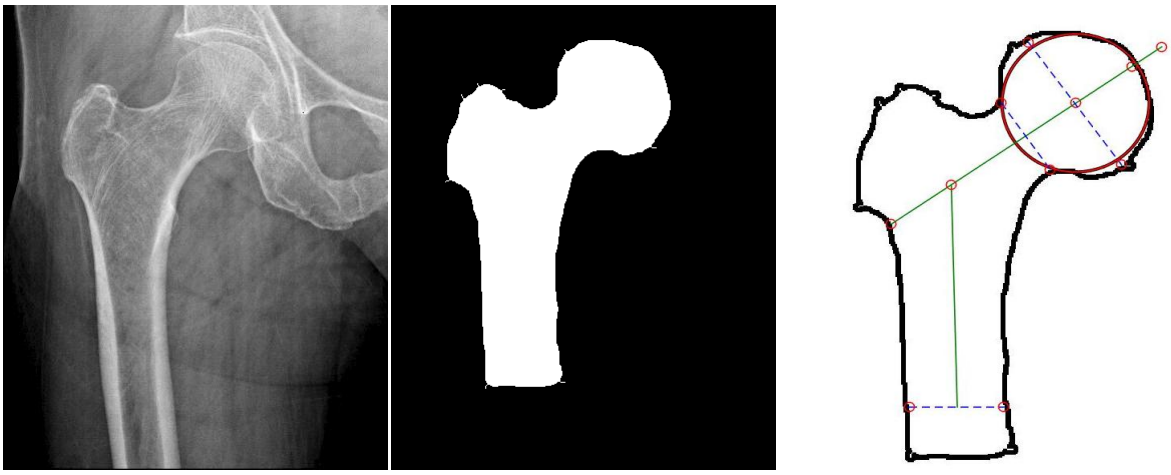

a) b) c)

Figure 4. Sample results of the experiment a) Input image b) Output from Active shape model c) detection of femur geometry using the proposed method

4.4 Performance metrics

The effectiveness of the proposed method is assessed through various metrics, including the error in femur volumetric estimation, classification accuracy, sensitivity, and specificity.

4.5 Competing methods

The comparison involves evaluating the proposed HSG-DBN method against existing approaches, specifically Deep Belief Network (DBN) [22], K-Nearest Neighbor (KNN) [24], Support Vector Machine (SVM) [25, 26], and Neural Network. In this analysis, the methods DBN, KNN, SVM, and NN are utilized as substitutes for the proposed HSG-DBN method employed in this research.

4.6 Performance analysis of the proposed classifier based on the features

Figure 5 illustrates the analysis of the proposed method based on the extracted features. For a training percentage of 0.9, the accuracy, as depicted in Figure 5a, achieved by the proposed method using femur (medical) features, image features, and combined features (medical + image) is 0.58, 0.8, and 0.9123, respectively. Figure 5b shows the sensitivity obtained by the proposed method with femur (medical) features, image features, and combined features, all yielding a value of 1. Furthermore, Figure 5c displays the specificity achieved by the proposed method using femur (medical) features, image features, and combined features, with values of 0.81, 0.87, and 0.965, respectively. Notably, the proposed method utilizing combined features outperforms in terms of accuracy, sensitivity, and specificity.

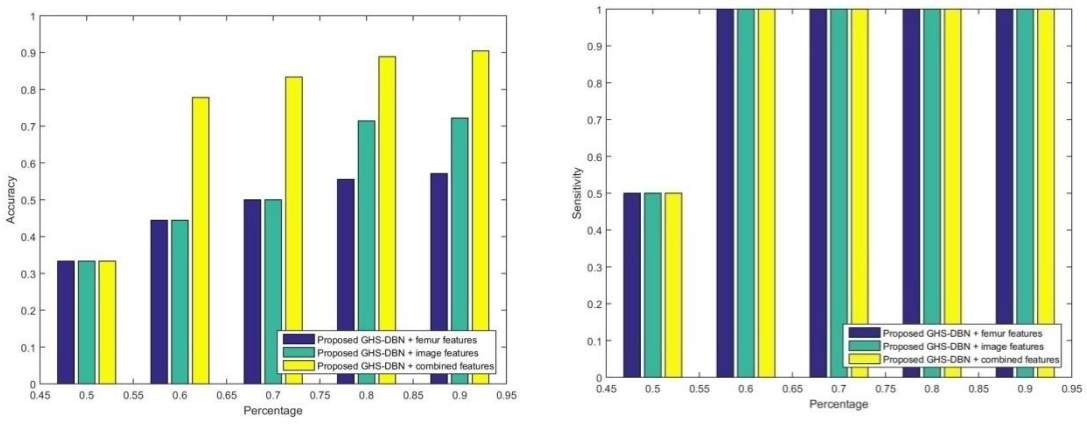

a) b)

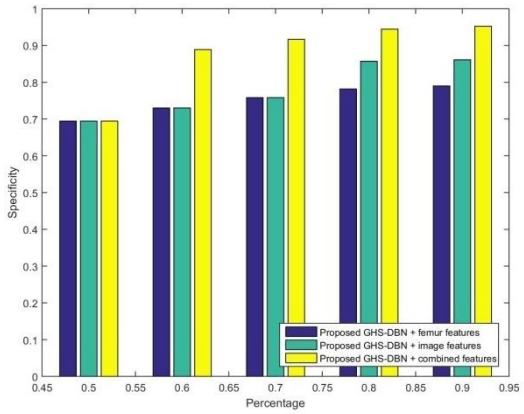

c)

Figure 5. Performance analysis based on features a) accuracy b) sensitivity c) specificity

4.7 Performance analysis of the proposed classifier based on volumetric estimation error

Figure 6 illustrates the volumetric estimation errors obtained from the proposed method for 50 images. In Figure 6a, the volumetric estimation errors for the first 25 images are presented, while Figure 6b displays the errors for images 25-50. Specifically, the volumetric errors for images 25 and 50 are measured at 0.8 and 1.231, respectively. The volumetric analysis involves a comparison of medical features derived from the proposed template method with the original features, emphasizing the need for minimal error in this process.

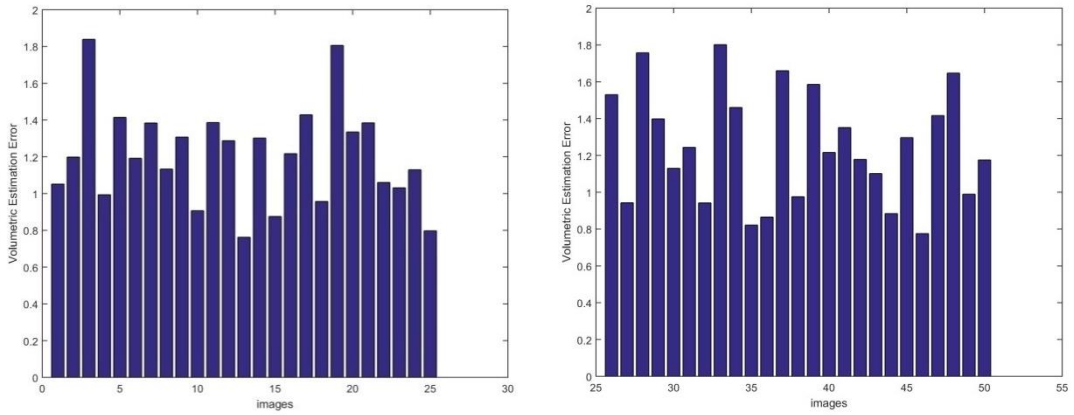

a) b)

Figure 6. Volumetric analysis a) for images 1-25 b) for images 25-50

4.8 Comparative Analysis based on training percentage

Figure 7 illustrates the analysis based on varying training percentages. For a training percentage of 0.9, the accuracy of different methods, including the proposed HSG-DBN, DBN, KNN, SVM, and NN, is determined to be 0.9724, 0.821, 0.9, 0.41, and 0.42, respectively. As depicted in Figure 7a, the accuracy of all methods demonstrates an increasing trend with higher training percentages, and notably, the proposed HSG-DBN exhibits the highest accuracy among them.

Examining sensitivity for the same training percentage, the proposed HSG-DBN, DBN, KNN, SVM, and NN exhibit values of 1, 1, 0.953, 1, and 0.599, respectively (Figure 7b). Similar to accuracy, sensitivity increases with higher training percentages, with the proposed HSG-DBN outperforming other methods in achieving greater sensitivity.

Furthermore, for a training percentage of 0.9, the specificity values for the proposed HSG-DBN, DBN, KNN, SVM, and NN are determined as 0.981, 0.91, 0.93, 0.712, and 0.7, respectively (Figure 7c). The trend across methods indicates an increase in specificity with higher training percentages. Notably, the proposed HSG-DBN demonstrates superior specificity compared to the other methods under consideration.

Figure 7. Comparative analysis of classification methods based on training percentage a) accuracy b) sensitivity c) specificity

4.9 Comparative Analysis based on kfold

Figure 8 presents the analysis based on k-fold validation. The accuracy values for various methods, including the proposed HSG-DBN, DBN, KNN, SVM, and NN, are observed as 0.888, 0.777, 0.444, 0.23, and 0.7111, respectively, for a k-fold value of 5. As depicted in Figure 8a, the accuracy of these methods exhibits an increasing trend with the rise in the k-fold value from 1 to 5. Notably, the proposed HSG-DBN demonstrates a higher accuracy compared to other methods. The sensitivity values for the methods (proposed HSG-DBN, DBN, KNN, SVM, and NN) are found to be 1, 1, 0.777, 0.7, and 0.656, respectively, for a k-fold value of 5. Illustrated in Figure 8b, the sensitivity of these methods shows an upward trend as the k-fold value increases from 1 to 5. The proposed HSG-DBN stands out with a higher sensitivity compared to alternative methods.

Examining the specificity values for the methods (proposed HSG-DBN, DBN, KNN, SVM, and NN) with a k-fold value of 5, they are determined as 0.87, 0.82, 0.66, 0.63, and 0.81, respectively. Shown in Figure 8c, the specificity of these methods follows an increasing pattern with the elevation of the k-fold value from 1 to 5. Notably, the proposed HSG-DBN exhibits a higher specificity compared to the other methods.

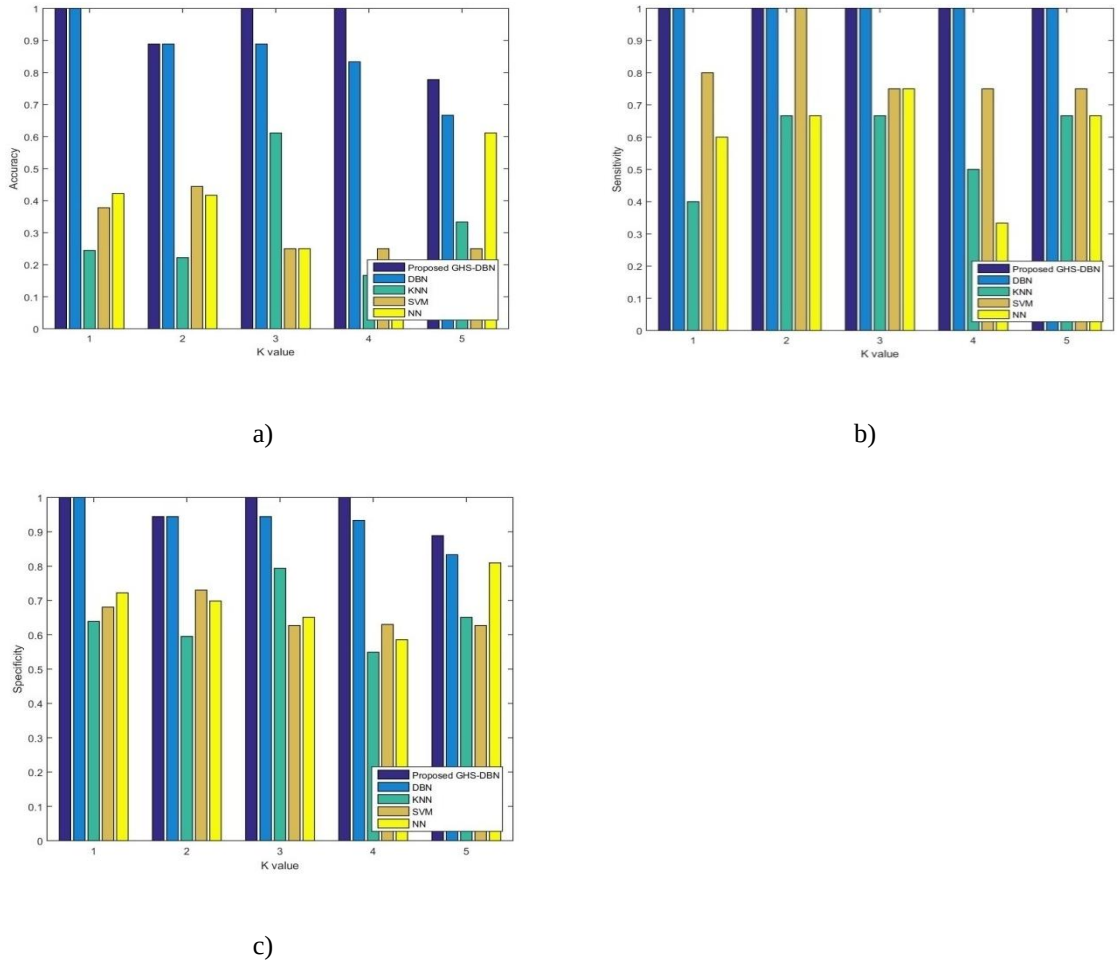

Figure 8. Comparative analysis of classification methods based on kfold a) accuracy b) sensitivity c) specificity

4.10 ROC analysis

In Figure 9, the ROC analysis for various classification methods is presented. At a 20% error rate, the True Positive Rate (TPR) for the proposed HSG-DBN is 0.8. In comparison, DBN, KNN, SVM, and NN achieved TPR values of 0.6, 0.31, 0.544, and 0.433, respectively. The proposed method demonstrates a superior TPR value for minimal error compared to existing methods.

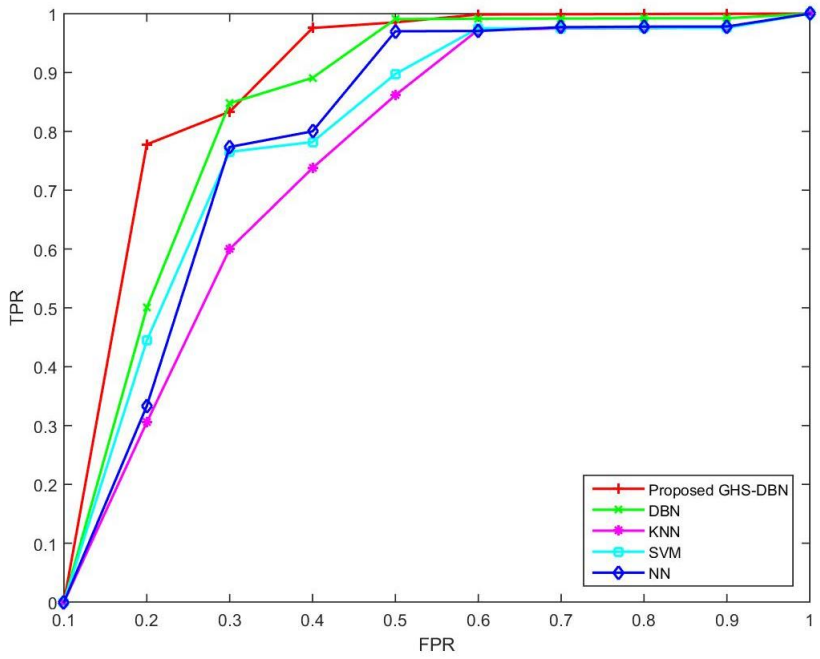

Figure 9. ROC analysis

4.11 Comparative discussion

Table 1 presents a comparative analysis of the methods, showcasing the performance metrics of the proposed method alongside existing approaches. The proposed method achieved notable accuracy, sensitivity, and specificity values, measuring at 0.967, 1, and 0.981, respectively. In contrast, the existing methods, including DBN, KNN, SVM, and NN, demonstrated varying levels of performance. DBN, KNN, SVM, and NN attained accuracy scores of 0.821, 0.9, 0.41, and 0.42, respectively. Sensitivity values for DBN, KNN, SVM, and NN were consistently high at 1, 1, 0.953, 1, and 0.599, respectively. Specificity results indicated that DBN outperformed the other methods with a score of 0.981, while KNN, SVM, and NN showed specificity values of 0.91, 0.93, and 0.712, and 0.7, respectively.

Table 1. Comparative discussion

	Proposed HSG-DBN	DBN	KNN	SVM	NN
Accuracy	**0.974**	0.821	0.9	0.41	0.42
Sensitivity	**1**	1	0.95	1	0.599
Specificity	**0.981**	0.91	0.93	0.71	0.71

5. Conclusion

The primary focus of this paper is the osteoporosis classification method employing the HSG-DBN, an integration of gradient descent and PSO algorithms for training the DBN. This integration enhances the efficiency and reduces complexity in classification by utilizing an effective feature vector derived from femur image analysis, specifically through Femur bone volumetric estimation. The initial step involves segmenting the input X-ray image using the active shape model to extract the femur's shape. Geometric estimation is then performed using the proposed template search method, identifying significant points on the femur. These geometric points serve as the basis for extracting medical-level features and subsequently, image-level features. The resulting effective features are fed into the DBN, determining the class label and ensuring accurate classification and decision-making. Experimental validation using a real-time database confirms the effectiveness of the classification method, demonstrating

improved accuracy. The proposed method achieves an accuracy of 0.9724, sensitivity of 1, and specificity of 0.981, substantiating its efficacy in osteoporosis classification.

Data Availability statement :
Upon corresponding author request.

References

[1] Jennifer S. Gregory, and Richard M. Aspden, "Femoral geometry as a risk factor for osteoporotic hip fracture in men and women," Medical engineering & physics, vol. 30, no. 10, pp. 1275-1286, 2008.

[2] Melih S. Aslan, Ahmed Shalaby, and Aly A. Farag, "Vertebral body segmentation using a probabilistic and universal shape model," IET Computer Vision, vol. 9, no. 2, pp. 234-250, 2015.

[3] Esther Pompe, Pim A. de Jong, Werner U. De Jong, Richard AP Takx, Anouk LM Eikendal, Martin J. Willemink, Matthijs Oudkerk, Ricardo PJ Budde, Jan-Willem J. Lammers, and Firdaus AA Mohamed Hoesein, "Inter-observer and inter-examination variability of manual vertebral bone attenuation measurements on computed tomography," European radiology, vol. 26, no. 9, pp. 3046-3053, 2016.

[4] Sami P. Vaananen, Lorenzo Grassi, Gunnar Flivik, Jukka S. Jurvelin, and Hanna Isaksson, "Generation of 3D shape, density, cortical thickness and finite element mesh of proximal femur from a DXA image," Medical image analysis, vol. 24, no. 1, pp. 125-134, 2015.

[5] V. Sapthagirivasan, M. Anburajan, and S. Janarthanam, "Extraction of 3D femur neck trabecular bone architecture from clinical CT images in osteoporotic evaluation: A novel framework," Journal of medical systems, vol. 39, no. 8, pp. 81, 2015.

[6] Alexandra Hotca, Shreyas Ravichandra, Artem Mikheev, Henry Rusinek, and Gregory Chang, "Precision of volumetric assessment of proximal femur microarchitecture from high-resolution 3T MRI," International journal of computer assisted radiology and surgery, vol. 10, no. 1, pp. 35-43, 2015.

[7] Ludovic Humbert, Yves Martelli, Roger Fonolla, Martin Steghöfer, Silvana Di Gregorio, Jorge Malouf, Jordi Romera, and Luis Miguel Del Río Barquero, "3D-DXA: Assessing the Femoral Shape, the Trabecular Macrostructure and the Cortex in 3D from DXA images," IEEE transactions on medical imaging, vol. 36, no. 1, pp. 27-39, 2017.

[8] Kiattisin Supaporn, and Chamnongthai Kosin, "Femur Bone Volumetric Estimation from a Single X-Ray Image for Osteoporosis Diagnosis," IEEE International Symposium on Communications and Information Technologies (ISCIT'06), pp. 1149-1152, 2006.

[9] R. N. Hiremath, A. K. Yadav, Sandhya Ghodke, Jyoti Yadav, Sumit Latwal, and Atul Kotwal, "Osteoporosis among household women: A growing but neglected phenomenon," Medical Journal Armed Forces India, pp. 1-6, 2016.

[10] Sheng-yong Wu, Hui-hui Jia, Didier Hans, Jing Lan, Li-ying Wang, Jing-xue Li, and Yue-zeng Cai, "Assessment of volumetric bone mineral density of the femoral neck in postmenopausal women with and without vertebral fractures using quantitative multi-slice CT," Journal of Zhejiang University SCIENCE B, vol. 10, no. 7, pp. 499-504, 2009.

[11] T. F. Lang, J. H. Keyak, M. W. Heitz, P. Augat, Y. Lu, A. Mathur, and H. K. Genant, "Volumetric quantitative computed tomography of the proximal femur: precision and relation to bone strength," Bone, vol. 21, no. 1, pp. 101-108, 1997.

[12] Jacqueline R. Center, Tuan V. Nguyen, Nick A. Pocock, and John A. Eisman, "Volumetric bone density at the femoral neck as a common measure of hip fracture risk for men and women," The Journal of Clinical Endocrinology & Metabolism, vol. 89, no. 6, pp. 2776-2782, 2004.

[13] L Sanchez-Riera, E Carnahan, T Vos, L Veerman, R Norman, S S Lim, D Hoy, E Smith, N Wilson, J M Nolla, J S Chen, M Macara, N Kamalaraj, Y Li, C Kok, C Santos-Hernandez, L March, "The global burden attributable to low bone mineral density," Annals of the rheumatic diseases, vol. 73, no. 9, pp. 1635-1645, 2014.

[14] Wilson JM, Jungner YG, "Principles and practice of mass screening for disease," World Health Organization, Geneva, 1968.

[15] E. Michael Lewiecki, Catherine M. Gordon, Sanford Baim, Mary B. Leonard, Nicholas J. Bishop, Maria-Luisa Bianchi, Heidi J. Kalkwarf et al., "International Society for Clinical Densitometry 2007 adult and pediatric official positions," Bone, vol. 43, no. 6, pp. 1115-1121, 2008.

[16] Markus B. Huber, Julio Carballido-Gamio, Jan S. Bauer, Thomas Baum, Felix Eckstein, Eva M. Lochmuller, Sharmila Majumdar, and Thomas M. Link, "Proximal femur specimens: automated 3D trabecular bone mineral density analysis at multidetector CT-correlation with biomechanical strength measurement," Radiology, vol. 247, no. 2, pp. 472-481, 2008.

[17] World Health Organization: WHO, taken from ""WWW.WHO.INT.", accessed on December 2017.

[18] Katie L. Stone, Dana G. Seeley, Li-Yung Lui, Jane A. Cauley, Kristine Ensrud, Warren S. Browner, Michael C. Nevitt, and Steven R. Cummings, "BMD at multiple sites and risk of fracture of multiple types: long-term results from the Study of Osteoporotic Fractures," Journal of Bone and Mineral Research, vol. 18, no. 11, pp. 1947-1954, 2003.

[19] Saskia van Engeland, Peter R. Snoeren, Henkjan Huisman, Carla Boetes, and Nico Karssemeijer, "Volumetric breast density estimation from full-field digital mammograms," IEEE transactions on medical imaging, vol. 25, no. 3, pp. 273-282, 2006.

[20] Andrzej Materka, Piotr Cichy, and Jerzy Tuliszkiewicz, "Texture analysis of x-ray images for detection of changes in bone mass and structure," Series in Machine Perception And Artificial Intelligence, vol. 40, pp. 189-196, 2000.

[21] Prithwish Chakraborty, Gourab Ghosh Roy, Swagatam Das, Dhaval Jain, Ajith Abraham, "An Improved Harmony Search Algorithm with Differential Mutation Operator", Fundamenta Informaticae - Swarm Intelligence, Vol. 95, No. 4, pp. 401-426, December 2009.

[22] J. Vojt, “Bc . Ján Vojt Deep neural networks and their implementation,” 2016.

[23] TFCootes, A Hill, C J Taylor, and J Haslam, " Use of active shape models for locating structures in medical images", Image and Vision Computing, vol.12, no.6, pp.355-365, July–August 1994.

[24] Zhenyun Deng, Xiaoshu Zhu, Debo Cheng, Ming Zong, and Shichao Zhang, " Efficient kNN classification algorithm for big data", Neurocomputing, vol.195, pp.143-148, 26 June 2016.

[25] Bernhard E. Boser, Isabelle M. Guyon, Vladimir N. Vapnik, "A training algorithm for optimal margin classifiers", in proceedings of the fifth annual workshop on Computational learning theory COLT '92, pp. 144-152, 1992.

[26] Shankar N, Sathish Babu, Viswanathan C "Femur bone volumetric estimation for Osteoporosis classification using Optimization based Deep Belief Network in X-ray images" computational intelligence, machine learning and data analytics the computer journal, 2019.